newborn score system. *Am. J. Dis. Child.*, **104**, 419–428.
DRAGE, J. S. and BERENDES, H. (1966) Apgar scores and outcome of the newborn. *Ped. Clin. of North Amer.*, **13**, 635–643.
DRAGE, J. S., KENNEDY, C., BERENDES, H., SCHWARTZ, B. K. and WEISS, W. (1986) The Apgar score as an index of infant morbidity. *Develop. Med. Child. Neurol.*, **8**, 141–148.
EFFER, S. B. (1969) Management of high-risk pregnancy. *Canadian Med. Assoc. J.*, **101**, 55–63.
ELDSTEIN, A. S., SCHULMAN, L. S. and SPRAFKA, S. A. (1979) *Medical Problem solving. An analysis of clinical reasoning.* Harvard University Press, London.
FELDSTEIN, M. S. (1965) A method for evaluating perinatal mortality risk. *Br. J. Prev. Soc. Med.*, **19**, 135–139.
GOODWIN, J. W., DUNN, J. T. and THOMAS, B. W. (1969) Antepartum identification of the fetus at risk. *Canadian Med. Assoc. J.*, **101**, 57–67.
HAERI, A. D., SOUTH, J. and NALDRETT, J. (1974) A scoring system for identifying pregnant patients with a high risk of perinatal mortality. *J. Obstet. Gynec. of the British Commonwealth*, **81**, 535–538.
HERNÁNDEZ, C. and ARIAS, J. E. (1984) Syntactic pattern recognition of fetal stress. *J. Biomed. Eng.*, **6**, 97–101.
HERNÁNDEZ, C. and GÓMEZ, L. (1984) Contextual analysis of fetal heart rate waveforms. Digital Signal Proc. North-Holland, 676–678.
HOBEL, C. J., HYVARINEN, M. A., OKADA, D. M. and OH, W. (1973) Prenatal and intrapartum high-risk screening. Prediction of the hi-risk neonate. *Am. J. Obstet. Gynecol.*, **117**, 1–9.
HULKKO, S. and KATAJA, M. (1982) Forecast model for the out come of a pregnancy. *Lecture Notes Medical Informatics*, 176–179.
KÜNZEL, W. (Ed.) (1985) *Fetal heart rate monitoring. Clinical practice and pathophysiology.* Springer-Verlag, Berlin, Heidelberg.
LEVENTHAL, L. A. (1979) 6502 *assembly language programming.* OSBORNE (Ed.), McGraw-Hill, London.
NELSON, K. B. and ELLENBERG, J. N. (1981) Apgar scores as predictors of chronic neurologic disability. *Pediatrics*, **68**, 36–44.
PARER, J. T. (1983) *Handbook of fetal heart rate monitoring.* W. B. Saunders Co., New York.
PAUL, R. H., PETRIE, R. H., RABELLO, Y. A. and MUELLER, E. A. (1981) Fetal intensive care. University of South California, Los Angeles.
REY, H. R., JAMES, L. S., FOX, H. E., DRISCOLL, J. M. and SHAMSI, H. (1984) A computer weighted scoring system for the prediction of fetal and neonatal outcome. *IEEE Eng. in Med. & Biol.*, **3**(3), 14–21.
ROLFE, P. (Ed.) (1986) *Fetal physiological measurements.* Butterworths, London.
SOKOL, R. J., ROSEN, M. G., STOJKOV, J. and CHI, K. L. (1977) Clinical application of high risk scoring on an obstetric service. *Am. J. Obstet. Gynecol.*, **128**, 652–661.

Communication

Depth discrimination in laser Doppler skin blood flow measurement using different lasers

A. N. Obeid D. M. Boggett N. J. Barnett G. Dougherty

Biomedical Instrumentation Centre, School of Engineering, Oxford Polytechnic, Gipsy Lane, Headington, Oxford OX3 0BP, UK

P. Rolfe

Bioengineering Unit, University of Oxford, John Radcliffe Hospital, Oxford OX3 9DU, UK

Keywords—*Blood flow, Doppler, Laser*

Med & Biol. Eng. & Comput., 1988, **26**, 415–419

1 Introduction

THE PRINCIPLE of Doppler broadening of the optical spectrum, when laser light is scattered from moving red blood cells (RBC) in skin tissue, has been successfully employed in a number of laser Doppler skin blood flow meters (BONNER and NOSSAL, 1981). The technique is particularly suitable for noninvasive, continuous monitoring in a number of clinical and research applications.

The most commonly reported laser source employed in skin blood flow laser Doppler flowmeters is the red helium/neon laser ($\lambda = 632{\cdot}8$ nm). It is generally acknowledged that, at this wavelength, the laser light penetrates relatively deeply into the dermis and even reaches underlying fatty subcutaneous tissues. The combined effect of absorption and scattering on the penetration depth of light through the skin has been studied in detail by a number of researchers for both *in vitro* and *in vivo* situations (ANDERSON and PARISH, 1981; WAN *et al.*, 1981). Results indicate that the penetration of red light in the skin can be anything from 600 μm to 1500 μm depending on the geometry of the tissue bed (ENKEMA *et al.*, 1981). This evidence suggests that a significant contribution to the laser Doppler signal is obtained from the deeper dermal region (where there is a large flux of RBC present) as well as from the capillary beds above the superficial dermal plexus (where the mean concentrations and velocity of RBCs is much smaller).

There are many instances in routine dermatology where the superficial dermal plexus alone is most affected by the presence of disease (e.g. psoriasis and eczema). In these situations it would be more useful to the clinician if the superficial dermal flow information could be isolated from the global dermal circulation (RYAN, 1985).

To discriminate between total and superficial skin blood flow it is necessary to select a suitable wavelength of laser light which will be preferentially absorbed and/or scattered in the upper dermis. One previous investigation (DUTEIL *et*

Professor Rolfe is now at Biomedical Engineering & Medical Physics, University of Keele, Thornburrow Drive, Hartshill, Stoke-on-Trent ST4 7QB, UK.

First received 22nd July 1987 and in final form 9th March 1988

al., 1985), has involved skin blood flow measurements using an He/Ne red laser ($\lambda = 632{\cdot}8$ nm) and an argon-ion laser ($\lambda = 457.9$ nm) operating with a complex optical feedback system to reduce noise and improve stability. In this study we have compared measurements of skin blood flow using an He/Ne 'green' laser operating at a wavelength of 543 nm, a standard He/Ne 'red' laser ($\lambda = 632{\cdot}8$ nm) and a near infra-red laser diode ($\lambda = 780$ nm). At the shorter (green) wavelength there is a marked increase in absorption and scattering in the dermis due to a number of factors. These include:

(*a*) In the epidermis, absorption by the presence of melanin rapidly increases as the wavelength decreases from $\lambda = 1200$ nm to 300 nm.

(*b*) In the dermis increased scattering towards shorter wavelengths from fibrous tissues (e.g. collagen fibres) is the most dominant mechanism in limiting the penetration depth of radiation.

(*c*) Absorption in the vascular bed is dominated by the presence of blood-borne pigmentation (e.g. haemoglobin and oxyhaemoglobin), of which there is a marked increase in absorption at 543 nm relative to the 'optical window' that exists at 633 nm.

The net result is that for near-infra-red light (800 nm) the penetration depth in fair Caucasian skin to a value of $1/e$ (37 per cent) of the incident energy density has been estimated to be approximately 1200 μm. The value for red light (600 nm) is approximately 550 μm, and the figure for green light may be as small as 150 μm (ANDERSON and PARISH, 1981).

2 System description

2.1 *In vitro measurements*

The purpose of this study was to compare the Doppler shift frequency spectra obtained for three different laser wavelengths under the same conditions of flow through a simple physical model. *In vitro* measurements were performed using a syringe-pumped model described in an earlier publication (BOGGETT *et al.*, 1986) in which a suspension of latex spheres and then blood (of known dilution) was passed through a single polythene tube (OD = 2·0 mm, ID = 1·0 mm). A block diagram of the experimental setup is shown in Fig. 1.

Using a 2 mW He/Ne laser as the red source (Hughes 3202H-PC), a 0·5 mW He/Ne laser (Melles Griot 05 LPL 344-1) as the green source and a 2 mW semiconductor laser diode (Sharp LT0 22 MC) as the near infra-red source, light from each of the three lasers was alternately directed on the surface of the rigidly supported polythene tube via the afferent optical fibre in the beam delivery probe (1 mm diameter plastic stepped-index type). The weak back-scattered laser light from the tube (containing both the frequency shifted and unshifted light) was collected by two efferent fibres within the probe. Photodetection was performed by a pair of sensitive silicon photodiodes (BPX 65) to reduce common mode noise signals (such as 50 Hz harmonics). The AC component of the photocurrent from the output of the photodiodes, containing the beat frequency Doppler signals, was then bandpass amplified (1 Hz–500 Hz) using a seventh-order cutoff filter.

Spectral analysis of the photocurrent signal was performed using a digital waveform analyser (DATA 6000, Data Precision). To obtain a reasonable signal-to-noise ratio (S/N) on the digitally processed photocurrent power spectra, averaging techniques were implemented in the frequency domain. Photocurrent power spectra were determined from the average of 25 512-point fast Fourier transforms (FFTs) at a sampling rate of 1 kHz. The total time interval required to obtain each averaged photocurrent spectrum was 30 s. Prior to recording spectra for the more powerful red and infra-red lasers, the output from each of these lasers was matched (as indicated by the DC response of the detector to the intensity of light reflected off the model) to that obtained from the (less powerful) green laser. Power spectra recorded on the digital waveform analyser were then saved on disk for further processing and analysis.

Having obtained photocurrent power spectra over a range of flow conditions for each laser, a flow index was computed following the technique employed by DUTEIL *et al.* (1985). Using a curve-fitting routine, a characteristic Doppler shift frequency (or flow parameter) was obtained by fitting the photocurrent power spectra to a single Lorentzian function of the form;

$$P(v) = A_1 \frac{\langle v_d \rangle}{\langle v_d \rangle^2 + v^2} + A_2 \qquad (1)$$

where $\langle v_d \rangle$, the mean shift or flow parameter, is the half-width at half-maximum (HWHM). A_1 is a quantity related to the number of scatterers in the small measuring volume under examination and A_2 is a constant related to detector and amplifier noise.

2.2 *In vivo measurements*

These measurements were concerned with obtaining

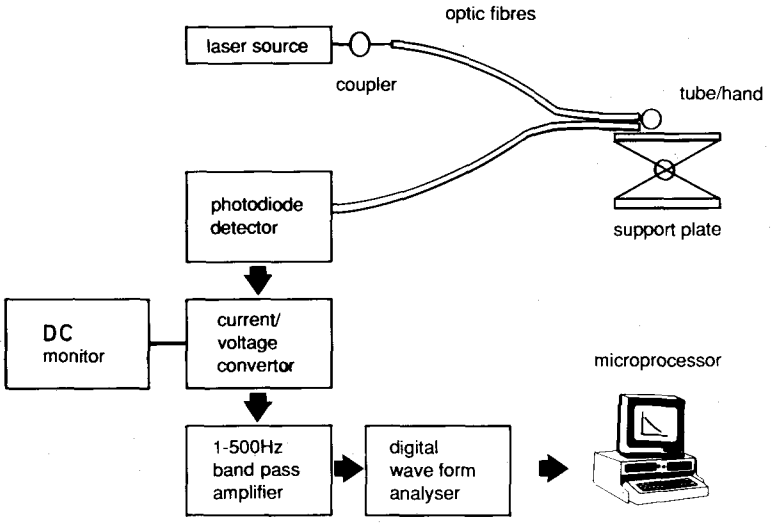

Fig. 1 *Block diagram of experimental setup*

power spectra of the low-frequency photocurrents which result from the photodetection of back-scattered laser light from the skin. Using the same optical and signal processing arrangement described above, light from each of the three lasers was alternately directed on to the surface of the skin. This was achieved by resting the hand in a specially constructed polyurethane mould (to minimise spurious movements) and then positioning the optic fibre probe to a constant measurement site on the forefinger.

Measurements of cutaneous blood flow were obtained over a range of skin surface temperatures for all three lasers. By switching the outputs from the three lasers into the optical-fibre beam delivery system, photocurrent beat frequency power spectra could be recorded for each skin blood flow situation. The time interval between taking consecutive measurements with the three laser systems was approximately 10 s. Recordings of skin surface temperature near the laser Doppler measurement site were obtained using a digital thermometer (Model 49TA, Yellow Springs Instrument Co. Inc.).

3 Results and discussion

3.1 *In vitro results*

Initially, *in vitro* flow measurements were obtained under conditions of zero flow for both latex spheres (diameter = 9·2 μm) and then fresh heparinised rat blood (concentration = 0·1 per cent volume fraction, diluted with physiological saline solution). Under no-flow conditions the Doppler frequency shifts in the power spectra arise only from the movement of particles (either latex spheres or RBC) under Brownian motion. The peak shapes of these spectra represent Lorentzians centred on the mean Doppler shift $\langle v_d \rangle$, which correspond to the mean velocities of the scatterers in the tube (Fig. 2). The frequency difference between the three curves in Fig. 2 is due to the wavelength dependence of the Doppler shift itself which, for a given particle velocity, is inversely proportional to the wavelength. Fitting eqn. 1 using a curve-fitting routine on a microprocessor we found that the equalities

$$\delta_{r-g} = \frac{v_g}{v_r} = \frac{\lambda_r}{\lambda_g}$$

$$\delta_{ir-g} = \frac{v_g}{v_{ir}} = \frac{\lambda_{ir}}{\lambda_g}$$

$$\delta_{ir-r} = \frac{v_r}{v_{ir}} = \frac{\lambda_{ir}}{\lambda_r}$$

were satisfied to a good approximation for both latex spheres and blood under Brownian motion. Actual and theoretical ratios obtained at the three wavelengths for both latex spheres and blood can be seen in Table 1.

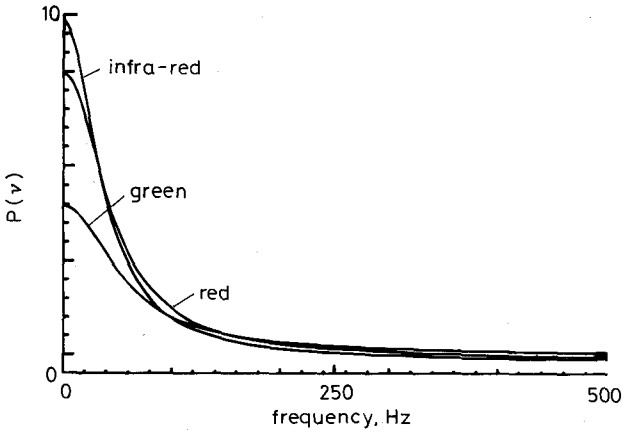

Fig. 2 *Lorentzian fits to averaged photocurrent power spectra recorded at the three different wavelengths for the Brownian motion of RBCs in the physical model. The results are for fresh heparinised rat blood diluted with saline solution (concentration = 0·1 per cent volume fraction)*

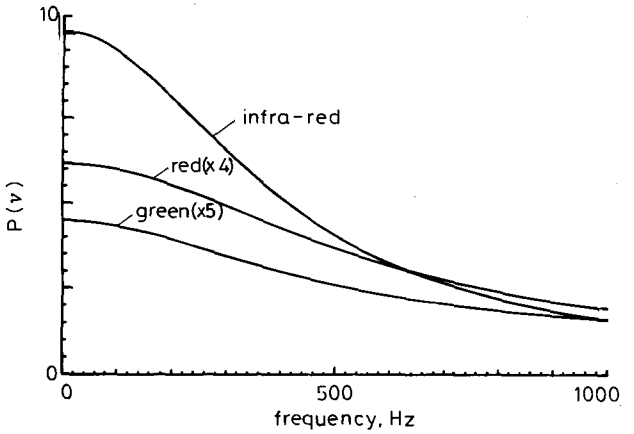

Fig. 3 *Lorentzian fits to averaged photocurrent spectra recorded at the three different wavelengths for blood flow in the physical model ($v = 2{\cdot}5\,mm\,s^{-1}$). The results are for fresh heparinised rat blood diluted with saline solution (concentration = 0·1 per cent volume fraction)*

Applying the same technique to flows of latex spheres and blood through the physical model ($v \simeq 2{\cdot}5\,mm\,s^{-1}$) we found that although the wavelength ratios obtained with latex spheres were in agreement with eqn. 2, the ratios computed for blood flow containing the green mean shift term $\langle v_d \rangle_g$ were much smaller than expected (Fig. 3 and Table 2). This seems to suggest a reduced penetrability of the green laser light in blood, in which most of the Doppler frequency shifting appears to be from the slower moving RBCs travelling on the outside of the flow (i.e. nearer the tube wall), thereby resulting in proportionally

Table 1 Mean shifts and ratios obtained for the Brownian motion of latex spheres and blood in the physical model

Mean shift	$\langle v_d \rangle \pm$ SD, latex	$\langle v_d \rangle \pm$ SD, blood	Ratio	Ratio, theoretical	Ratio ± SD, latex	Ratio ± SD, blood
$\langle v_d \rangle_g$	66·8 3·8	20·2 2·6	$\langle v_d \rangle_g / \langle v_d \rangle_r$	1·17	1·1 0·1	1·4 0·4
$\langle v_d \rangle_r$	58·8 2·9	14·3 0·9	$\langle v_d \rangle_g / \langle v_d \rangle_{ir}$	1·44	1·4 0·1	1·7 0·4
$\langle v_d \rangle_{ir}$	48·4 3·2	11·8 0·4	$\langle v_d \rangle_r / \langle v_d \rangle_{ir}$	1·23	1·2 0·1	1·2 0·1

Table 2 Mean shifts and ratios obtained for flows of latex spheres and blood through the physical model ($v = 2{\cdot}5\,mm\,s^{-1}$)

Mean shift	$\langle v_d \rangle \pm$ SD, latex	$\langle v_d \rangle \pm$ SD, blood	Ratio	Ratio, theoretical	Ratio ± SD, latex	Ratio ± SD, blood
$\langle v_d \rangle_g$	311 14	203 52	$\langle v_d \rangle_g / \langle v_d \rangle_r$	1·17	1·1 0·1	0·4 0·1
$\langle v_d \rangle_r$	278 19	461 41	$\langle v_d \rangle_g / \langle v_d \rangle_{ir}$	1·44	1·2 0·2	0·5 0·1
$\langle v_d \rangle_{ir}$	255 14	412 19	$\langle v_d \rangle_r / \langle v_d \rangle_{ir}$	1·23	1·1 0·1	1·1 0·1

smaller values for $\langle v_d \rangle_g$. The reduced penetration depth of green light is consistent with our own spectrophotometric data which estimate that the absorptivity due to blood-borne pigmentation (e.g. haemoglobin and oxy-haemoglobin) increases by almost 40 per cent from red ($\lambda = 600$ nm) to green ($\lambda = 543$ nm). Under zero-flow conditions in blood, reduced penetrability effects could not be expected to be observed for the green laser, as, under RBC Brownian motion, a homogeneous distribution of velocities exists right across the tube. In this situation, each laser system will 'see' the same velocity profile regardless of the absorptivity of the blood (the relative magnitude of the spectra, however, will be affected). For flows of latex spheres, all the values of $\langle v_d \rangle$ are in accordance with the theoretically derived figures (Table 2). This is because absorption losses in the latex spheres suspension are small compared with the blood solutions—any reduced penetrability will therefore equally affect all three laser systems.

3.2 *In vivo results*

Low-frequency photodetector power spectra covering the range 1–500 Hz were recorded for green, red and infra-red laser light scattered from the forefingers of three healthy Caucasian adult male subjects. By collecting the back-scattered light from a static surface reflector, baseline noise spectra were also obtained. In all three types of measurements the detected laser power, as indicated by the DC output voltage of the photodiode, was the same. The measurements were repeated several times for each wavelength to check the reproducibility of the method. Fig. 4 shows the typical photocurrent power spectra obtained using each laser from the same measurement site on the forefinger. Apart from the baseline noise signals (which were of equal magnitude) the spectra have very different characteristics. In Table 3, the ratios of the mean frequency shifts

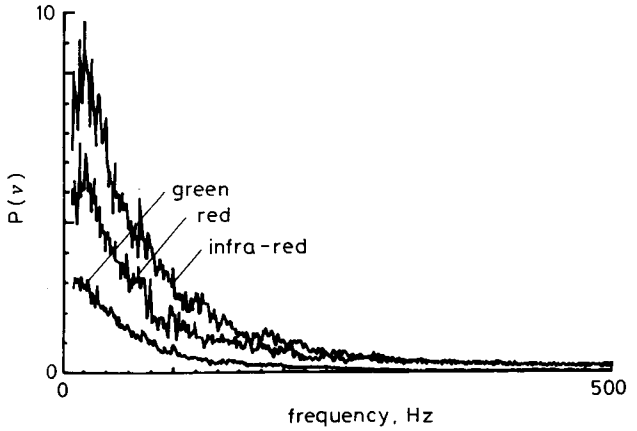

Fig. 4 *Photocurrent power spectra obtained from the forefinger for all three laser systems in the range 0–500 Hz. For each recording, the laser output was adjusted to give the same reflected light intensity from the skin (as indicated by the DC response of the photodiode). The skin surface temperature in each case was maintained at 27·3°C*

$\langle v_d \rangle$ have been calculated for each wavelength over a range of skin surface temperatures. The mean frequency shift ratios clearly show the detection of skin blood flow using the red and near-infra-red lasers consistently produces the broadest power spectra. This is in sharp contrast with the relatively narrow range of Doppler frequency shifts obtained with the green He/Ne laser.

The power spectra obtained with the near-infra-red laser (780 nm) and red laser (633 nm) depict a situation in which the relatively high Doppler frequency shifts can be attributed to a combination of multiple scattering (produced by successive Doppler shifts occurring in high RBC concentration environments) and/or to a significant proportion of RBCs moving at high velocities. With the green laser (543 nm), however, there is a significant absence of high-frequency contributions in the photocurrent spectrum. This suggests that the effect of multiple scattering is negligible and/or that the numbers of RBCs moving at high mean velocities are smaller. On this basis, the characteristics of the photocurrent power spectra recorded with the green laser, are consistent with a response solely limited to RBC activity in the capillary beds and upper papillary plexus. The frequency difference between the near-infra-red and red spectra shown in Fig. 4 and the ratios of the calculated mean shifts shown in Table 3 are due to the wavelength dependence of the Doppler shift itself.

4 Conclusion

A comparison of the photocurrent spectral response of the three laser systems for both *in vivo* and *in vitro* blood flow situations shows the significantly reduced response of green laser light to blood flow. The characteristics of the photocurrent spectra obtained using the green laser are consistent with a response limited to blood flow in the capillary beds and the upper papillary-plexus, where the concentration and mean velocity of moving RBCs is small. Our *in vitro* measurements support the fact that the reduced penetrability of green light in skin tissue can be partially attributed to absorption by pigments in the blood itself, although increased scattering from structures within the dermis could be the more dominant mechanism. For the *in vivo* measurements, the ratio of the mean frequency shift obtained for the infra-red source to that of the red source was approximately equal to the ratio of the optical frequencies. This suggests that the collected light for both sources is coming from approximately the same volume of tissue, even though the near-infra-red light possibly penetrates more deeply.

There are practical difficulties associated with using the green He/Ne laser for depth discrimination studies because of its low power (manifested in reduced reflection and net back-scatter from the skin), which makes detection and subsequent electronic processing of the Doppler signals difficult. It was, however, found to be stable and low noise, avoiding the need for a costly optical feedback stabilisation system, and represents an attractive, low-cost alternative to an argon-ion laser.

Table 3 In vivo measurements of mean frequency shifts and ratios obtained from a constant measurement site on the forefinger. The results shown were obtained from the same subject over a range of skin surface temperatures. Three sets of measurements were taken for each laser system at each skin surface temperature indicated

	Mean shifts			Ratios of mean frequency shifts				
Laser	$\langle v_d \rangle \pm$ SD, $t = 29$°C	$\langle v_d \rangle \pm$ SD, $t = 32$°C	$\langle v_d \rangle \pm$ SD, $t = 33$°C	Ratio	Ratio, theoretical	Ratio ± SD, $t = 29$°C	Ratio ± SD, $t = 32$°C	Ratio ± SD, $t = 33$°C
Green	27·3 3·1	57·6 9·2	59·4 9·2	$\langle v_d \rangle_g / \langle v_d \rangle_r$	1·17	0·69 0·68	0·77 0·17	0·90 0·13
Red	39·6 0·2	74·5 11·1	66·3 1·1	$\langle v_d \rangle_g / \langle v_d \rangle_{ir}$	1·44	0·83 0·09	0·98 0·16	0·95 0·18
Infra-red	33·6 0·4	58·7 2·6	62·7 7·9	$\langle v_d \rangle_r / \langle v_d \rangle_{ir}$	1·23	1·18 0·01	1·27 0·20	1·06 0·13

Acknowledgments—We would like to acknowledge Peter Grebenik, Chemistry Department, Oxford Polytechnic, for supplying the curve-fitting program and for his helpful advice.

References

ANDERSON, R. R. and PARISH, P. (1981) The optics of human skin. *J. Invest. Derm.*, **77**, 13–19.

BOGGETT, D., OBEID, A., BLOND, J. and ROLFE, P. (1986) Calibration of a laser Doppler skin blood flow meter using a simple fluid model and digital signal processing. In *Electronics in medicine and biology—selected papers*. COPELAND, K. (Ed.), IERE, London, 241–247.

BONNER, R. and NOSSAL, R. (1981) Model for laser Doppler measurements of blood flow in tissue. *Appl. Optics*, **20**, 2097–2107.

DUTEIL, L., BERNENGO, J. C. and SCHALLA, W. (1985) A double wavelength laser Doppler system to investigate skin microcirculation. *IEEE Trans.*, **BME-32**, 439–447.

ENKEMA, L., HOLLOWAY, D., PIRAINO, D. D., HARRY, D., ZICK, G. L. and KENNY, M. A. (1981) Laser Doppler velocimetry vs heater power as indicators of skin perfusion during transcutaneous O_2 monitoring. *Clin. Chem.*, **27**, 391–396.

RYAN, T. J. (1985) Dermal vasculature. In *Methods in skin research*. SKERROW, D. and SKERROW, C. J. (Eds.) J. Wiley & Sons, Chichester, 527–558.

WAN, S., ANDERSON, R. R. and PARISH, P. (1981) Analytical modeling for optical properties of the skin with *in vitro* and *in vivo* applications. *Photochem. Photobiol.*, **34**, 493–499.

Communication

Optimal design of mechanical ventilator waveform using a mathematical model of the ventilatory system

S. A. Ben-Haim

Cardiovascular Research Group, Rappaport Family Institute for Research in the Medical Sciences, Department of Physiology & Biophysics, Technion-Israel Institute of Technology, 2 Efron Street, PO Box 9697, Haifa, Israel

U. Dinnar

Heart System Research Center, Julius Silver Institute of Biomedical Engineering, Department of Biomedical Engineering, Technion-Israel Institute of Technology, Haifa 32000, Israel

G. M. Saidel

Department of Biomedical Engineering, Case Western Reserve University and Veterans Administration Medical Center, Cleveland, OH 44106, USA

Keywords—*Artificial ventilation, Chest wall dynamics, Emphysema, Mathematical model, Restrictive lung disease*

Med. & Biol. Eng. & Comput., 1988, **26**, 419–424

List of symbols

Variables

A area
P pressure (force/area)
V volume
Z airway resistance function
σ stress (force/area)
ϕ area ratio, a_{rl}/a_{rc}
ρ density
X_i distance of structure i
ΔX_i displacement from operating point of structure i

Parameters

K_{1i}, K_{2i}, K_{3i}, K_{4i} empirical constants of pressure/displacement relationship of structure

Subscripts

a alveolar
ab abdominal
ao airway opening
aw airway
di diaphragm
lt lung
rc ribcage
rl lung apposed ribcage

First received 13th October 1987 and in final form 11th March 1988

1 Introduction

MECHANICAL VENTILATION of the lungs is intended to assure adequate gas exchange with minimal side effects on other physiological functions. Clinically, an empirical approach is taken in the application of mechanical ventilation. With this approach, therapy often fails to restore normal pulmonary function and may have deleterious side effects especially in the presence of severe pulmonary dysfunction (e.g. patients with pulmonary failure). Rational application of therapies requires an understanding of the physiological effects of different ventilatory patterns. As an

alternative to an empirical approach, one can use information from simulation studies with a suitable mathematical model of the respiratory system.

Previous studies have examined such variables as the shape of the respiratory waveform (ADAMS *et al.*, 1970; BERGMAN, 1967; 1969; DAMMAN *et al.*, 1978), inspiratory-to-expiratory ratio (SYKES and LUMLEY, 1969; LUMLEY *et al.*, 1969), inspiratory flow rate (OWEN-THOMAS *et al.*, 1968; FAIRLY and BLENKARN, 1966; BARBINI, 1982) and airway-opening pressure (BERGMAN, 1984; 1963; BOROS, 1979) using pneumatic lung analogues (BARBINI, 1982; BERGMAN, 1984; CAMPBELL and BROWN, 1963; RATTENBORG and HOLADAY, 1966; JANSSON and JONSON, 1972) and artificially ventilated adults with some type of pulmonary disease (DAMMAN *et al.*, 1978; BARBINI, 1982). The results of these studies have been inconclusive in several ways. Although circulatory and respiratory changes were found as a consequence of altering inspiratory waveforms, no physiological interpretation can be drawn because of inadequacies of the underlying models. Furthermore, the extent of side effects of positive-pressure ventilation cannot be quantified in relation to a specific mode of ventilation. Thus, no clinical recommendations can be drawn from these investigations.

Generally speaking, in the process of applying positive airway pressure to increase the lung volume and improve ventilation, the pressure produced across the lungs and in the chest cavity can lead to barotrauma and depressed cardiovascular function. As a consequence of an increased intrathoracic pressure

(*a*) the reflex activation of baroreceptors causes increased secretion of antidiuretic hormone and changes in cardiovascular reactivity (HEMMER *et al.*, 1980; VIQUERAT *et al.*, 1983)
(*b*) increased impedance to the venous return produces a decrease in cardiac filling (QVIST *et al.*, 1975; LUCE, 1984)
(*c*) all cavities of the heart are compressed and ventricular volumes are decreased (VIQUERAT *et al.*, 1983; CASSIDY and RAMANATHAN, 1984).

The pressure transmitted to the mediastinum by artificial ventilation reduces cardiac output and results in hypoperfusion of the peripheral organs. The decreased perfusion pressure of these organs (i.e. the difference between the mean arterial and venous pressure) can impair cerebral, renal and hepatic function (HALL *et al.*, 1974; JOHNSON *et al.*, 1977).

In this study, we will provide a quantitative analysis of the respiratory pressures produced by various inspiratory waveforms in normal and pathological conditions. The basis for this is a detailed mathematical model of chest wall mechanics that describes the dynamic, nonlinear mechanics of the ventilatory system in terms of the major mechanical elements: ribcage, abdomen, diaphragm and lung (BEN-HAIM and SAIDEL, 1987). Consequently, the model can predict pressures in the lung and chest cavity from which we can assess the pulmonary and cardiovascular side-effects. Using input waveforms corresponding to volume-driven and pressure-driven mechanical ventilation, we shall simulate the pressures produced in subjects with normal and diseased lungs.

2 Passive chest wall model

The chest wall is formed by fixed and mobile parts. The fixed parts consist of the vertebral column, clavicle and the pelvis. The ribcage and the abdominal wall form the movable parts of the chest wall. The diaphragm separates the pleural and abdominal cavities. The mobile surfaces of the pleural cavity consist of the lung-apposed portions of the ribcage and the diaphragm. The abdominal cavity has the following mobile surfaces:

(*a*) lung-apposed portion of the diaphragm
(*b*) zone of apposition, which consists of the ribcage-apposed portion of the diaphragm (MEAD and LORING, 1982)
(*c*) ventral abdominal wall not tented by the ribcage.

Our model incorporates these basic features of a chest wall structure as shown in Fig. 1. The chest wall is divided into ribcage, diaphragm and abdominal compartments. We lump all movable parts of the ribcage and the abdominal wall into a membrane attached to a fixed skeleton. Forming the ribcage membrane (RC), are the lung-apposed ribcage and the diaphragm-apposed ribcage membranes. The ventral abdominal wall caudal to diaphragm insertions (AB) forms a second external chest wall

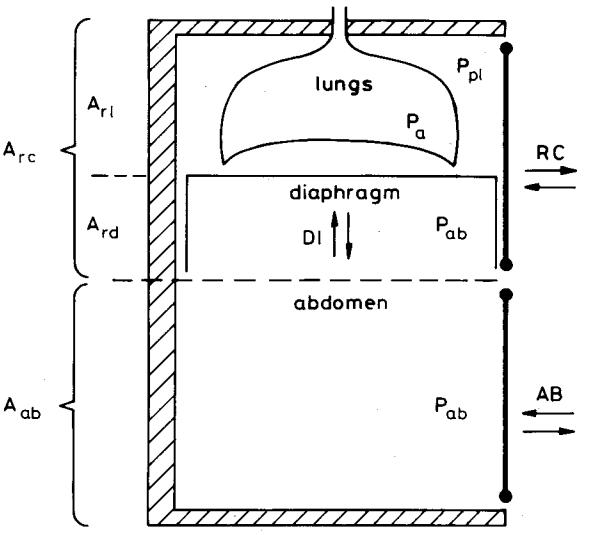

Fig. 1 *Model representation of chest wall structure*

membrane. The diaphragm (DI), which separates the pleural space from the abdominal cavity, is conceptualised to move in the direction parallel to the chest wall surface. In contrast the chest wall membranes RC and AB, are conceptualised to move perpendicular to the chest wall surface. The projected surface areas of the rib cage A_{rc} and of the abdominal cavity A_{ab} are constant, but the projected area of the lung-apposed ribcage A_{rl} is dependent on the diaphragm position.

As lateral chest wall movement is negligible, a change in the area ratio of the lung apposed rib-cage in the diaphragm-apposed ribcage, $\phi = A_{rl}/A_{rc}$, is proportional to the displacement of the diaphragm from its insertions. For standing adults we can consider the chest wall to be stiff so that the lung-apposed ribcage and the diaphragm-apposed ribcage are moving together with no relative displacement (GOLDMAN and MEAD, 1973). In this case the two external displacements are the changes in ribcage A-P distance X_{rc}, and the abdominal wall A-P distance X_{ab}.

The chest model described here is a special case of a general model of chest wall mechanics developed by us (BEN-HAIM and SAIDEL, 1987). The volume of the lung is the volume of the pleural cavity that it fills:

$$V_l = \phi A_{rc} X_{rc} \tag{1}$$

Because the abdominal contents are essentially incompressible, any inward displacements of the surrounding container must equal outward displacements elsewhere:

$$\Delta[X_{ab} A_{ab}] - \Delta[(1 - \phi)(X_{rc} A_{rc})] = 0 \tag{2}$$

2.1 *Mass balance*

The gas contained within the lung is compressed by the alveolar pressure P_a. A mass balance equation for the gas moving in the airways is

$$\frac{d\rho_l V_l}{dt} = \rho_{ao} Q_{ao} \tag{3}$$

where ρ_l and ρ_{ao} are the densities of the gas in the lung and at the airway opening. From the ideal gas law, we obtain

$$\rho = \frac{P}{RT/M} \tag{4}$$

where M is the molecular weight of gas, R is the ideal gas constant and T is the absolute temperature. Substituting eqn. 4 into eqn. 3 and neglecting the small changes of RT/M, we obtain

$$\frac{d(P_a V_l)}{dt} = Q_{ao} P_{ao} \tag{5}$$

After expanding the derivative and rearranging eqn. 5 we find that

$$Q_{ao} = \frac{1}{P_{ao}}\left[V_l \frac{dP_a}{dt} + P_a \frac{dV_l}{dt}\right] \tag{6}$$

2.2 *Mechanical balances*

We can express the difference between the alveolar pressure and the pressure in the airway opening in terms of an airway resistance function:

$$P_{ao} - P_a - Z_{aw}(Q_{ao}) = 0 \tag{7}$$

where Z_{aw} is an airway resistance function.

The alveolar pressure P_a acts on the internal side of the alveoli whereas the pleural pressure P_{pl} acts on the pleural surface of the lungs.

Therefore, the pressure balance for the lung tissue is

$$P_a - P_{pl} - \sigma_{lt}(V_l) = 0 \tag{8}$$

Opposing the action of the pleural pressure P_{pl} and the abdominal pressure P_{ab} is the passive stress $\sigma_{rc}(X_{rc})$. Therefore, the pressure balance for the ribcage is

$$\phi P_{pl} + (1 - \phi)P_{ab} - \sigma_{rc}(X_{rc}) = 0 \tag{9}$$

where we have assumed that the interaction stress between the ribcage and the abdomen can be neglected (BEN-HAIM and SAIDEL, 1987). Similarly, the pressure balance for the abdominal wall is

$$P_{ab} - \sigma_{ab}(X_{ab}) = 0 \tag{10}$$

and for the diaphragm is

$$P_{ab} - P_{pl} - \sigma_{di}(\phi) = 0 \tag{11}$$

2.3 *Constitutive relationships*

We used the Roher equation for approximation of airway resistance function:

$$Z_{aw} = K_{1aw} Q_{ao} + K_{2aw} |Q_{ao}^4| Q_{ao} \tag{12}$$

where K_{1aw}, K_{2aw} are chosen empirically to fit the data from the literature (ROHER, 1915; RAHN *et al.*, 1946).

A hyperbolic relationship is assumed between the stress and displacement; a linear relationship is assumed between the stress and the velocity; and the inertial stresses were neglected for each membrane (BEN-HAIM and SAIDEL, 1987):

$$\sigma_j(X_j) = K_{1j} \sinh K_{2j}(\Delta X) + K_{3j} \frac{dX_j}{dt} + K_{4j} \tag{13}$$

where X_j represents X_{rc}, X_{ab}, ϕ and V_l. The stress $\sigma_j(X_j)$ represents σ_{rc}, σ_{di}, σ_{ab} and σ_{lt}. The parameters K_{1j}, K_{2j}, K_{3j} and K_{4j} define the shape of the relationship.

3 Simulation studies

The variables of the chest wall model comprising eqns. 1 and 2 and 6–11 are the pressures P_{ao}, P_a, P_{pl} and P_{ab}, the A-P distances X_{rc} and X_{ab}, the area ratio ϕ and the lung volume V_l and its time derivative Q_{ao}.

The model parameter values listed in Table 1 were chosen to match the normal, human experimental data (BEN-HAIM and SAIDEL, 1987; MEAD and LORING, 1982; GOLDMAN and MEAD, 1973; RAHN *et al.*, 1946). The parameter values for lung tissue (K_{1lt}, K_{2lt}) were increased or decreased by 40 per cent to simulate an expected emphysematous and restrictive lung behaviour. Altering the parameter values in this way simulates lung tissue pathologies specifically, i.e. restrictive and emphysematous conditions were modelled by high and low lung compliance, respectively, but airway resistance was unaltered.

Table 1 Parameter values

Parameter	*rc*	*ab*	*di*	*lt*	*aw*
K_1	5·1	1·2	100·0	0·5 (0·3) [0·7]	1·6
K_2	1·0	1·0	1·0	1·0 (0·6) [1·4]	1·2
K_3	20·0	4·0	200·0	4·0	–
K_4	0·0	1·0	6·0	0·0	–

( ): emphysematous; [ ]: restrictive
Area values: $A_{rc} = 0{\cdot}4$; $A_{ab} = 0{\cdot}8$

We simulated the effects of mechanical ventilation with positive pressure inspiration and passive expiration assuming no active forces. For simulating pressure ventilators, $P_{ao}(t)$ is the specified input waveform during inspiration. For simulating volume ventilators, $Q_{ao}(t)$ is the specified input waveform during inspiration. These input waveforms (Fig. 2) are the sinusoids, square, ascending ramp, descending ramp and triangle. We adjusted the amplitude of each inspiratory wave so that the cycle tidal volume was 1·0 litre. The period of each cycle was 6 s in all simulations, of which half was used for passive expiration. This provides a common basis for comparison.

For all simulations, we solved the system of eqns. 1, 6–11 by using sixth-order Runga-Kutta algorithm. Given arbitrary initial values, the solution was continued until a steady state was achieved. These solutions were independent of the initial values.

Because the pleural pressure is acting on the cardiovascular system, we measured the inspiratory cycle integral of the pleural pressure:

$$PCI = \int P_{pl}\, dt \tag{14}$$

This integral conveys information about positive pressures induced by artificial ventilation, which would be expected to produce cardiovascular side effects. With respect to pulmonary side effects, especially barotrauma, peak airway and alveolar pressures were considered as predictors.

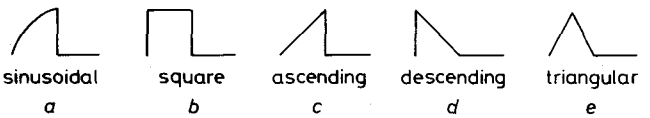

Fig. 2 *Waveforms used in the simulation studies: (a) sinusoidal, (b) square, (c) ascending ramp, (d) descending ramp, (e) triangular waveform*

4 Results

4.1 *Pressure ventilator*

To achieve the required ventilation pattern, the pressure-driven ventilation was simulated with a P_{ao} ranging between 20 and 60 cm of H_2O for normal lungs depending on the waveform used. Fig. 3 displays the peak

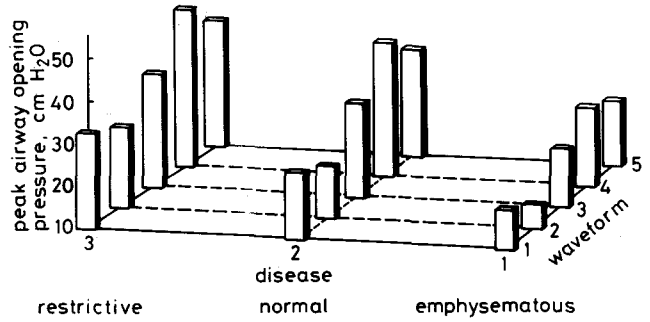

Fig. 3 *Pressure ventilator: peak airway opening pressure cm H_2O. Waveforms: 1: sinusoid; 2: square; 3: ascending; 4: descending; 5: triangular*

airway pressure induced by the pressure ventilator for normal, restrictive and emphysematous lungs. The minimal peak airway pressure was achieved using a square waveform regardless of the lung condition. The peak airway pressure of the restrictive lung model was higher than those of the emphysematous and normal lung models.

Fig. 4 shows the peak pleural pressure (PPP) above the resting pleural pressure. For normal or restrictive lung models we find a minimum PPP with a sinusoid and maximum PPP with the descending ramp. The minimum PPP for the emphysematous lung occurred with the square waveform, but the PPP of the sinusoid was just a little larger. The maximum PPP was achieved using a descending ramp.

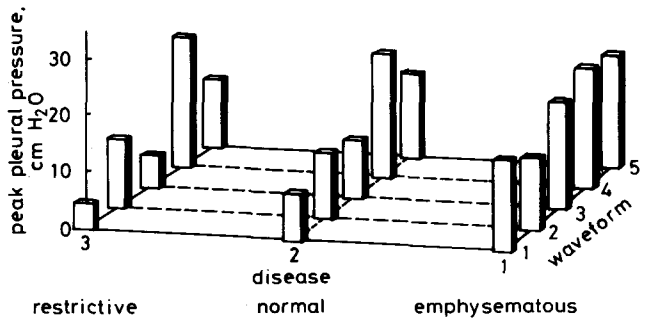

Fig. 4 *Pressure ventilator: peak pleural pressure, cm H_2O. Waveforms: 1: sinusoid; 2: square; 3: ascending; 4: descending; 5: triangular*

The inspiratory pleural pressure cycle integral (PCI) was lower with the restrictive lung model than with the normal or emphysematous lung regardless of the waveform used (Fig. 5). For normal, restrictive and emphysematous lungs the PCI index was the lowest with the ascending ramp, but the sinusoidal waveform was almost as low. The key results are summarised in Table 2.

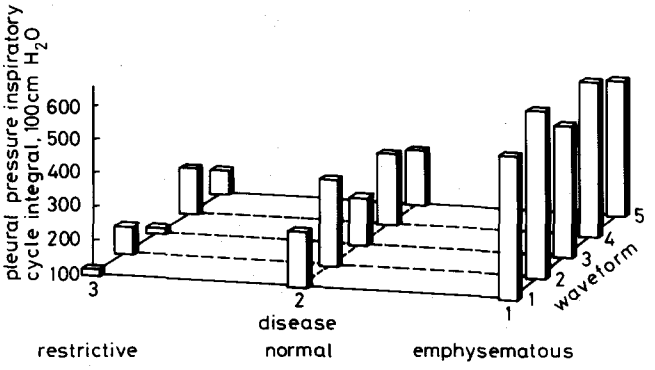

Fig. 5 *Pressure ventilator: inspiratory pleural pressure positive cycle integral, 100 cm H_2O s. Waveforms: 1: sinusoid; 2: square; 3: ascending; 4: descending; 5: triangular*

4.2 *Volume ventilator*

Volume-driven ventilation was simulated with an input Q_{ao} whose peak value varied between 12 and 30 l min^{-1} among the different waveforms. Fig. 6 displays the peak airway flow (PAF) produced by these waveforms. For normal, restrictive and emphysematous lung models, the minimum PAF was achieved using a square waveform. Maximum peak airway pressure (PAP) occurred with application of an ascending ramp, with the descending ramp causing the lowest PAP (Fig. 7) although the square waveform was almost as low. For all lung models the PPP is a minimum with the descending ramp and maximum with the ascending ramp (Fig. 8). Generally, PPP was higher for the emphysematous model than for the normal and restrictive models of the lung.

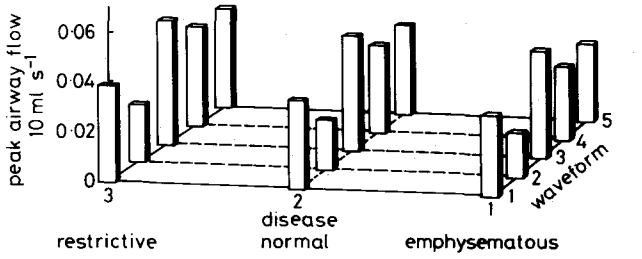

Fig. 6 *Volume ventilator: peak airway opening flow, 10 ml s^{-1}. Waveform: 1: sinusoid; 2: square; 3: ascending; 4: descending; 5: triangular*

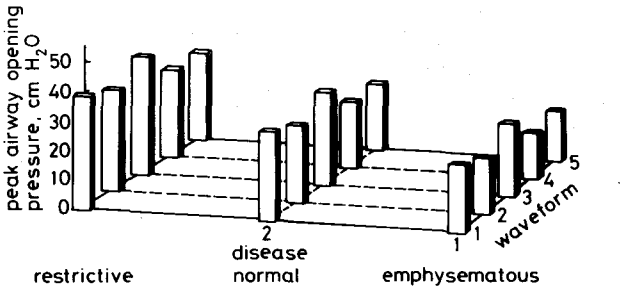

Fig. 7 *Volume ventilator: peak airway opening pressure, cm H_2O. Waveforms: 1: sinusoid; 2: square; 3: ascending; 4: descending; 5: triangular*

Table 2 Pressure ventilator

		Lung model		
Parameter	Value	Emphysematous	Normal	Restrictive
Peak airway pressure	minimum	square	square	square
	maximum	descending	descending	descending
Positive pleural pressure integral	minimum	ascending	ascending	ascending
	maximum	square	square	square

Table 3 Volume ventilator

Parameter	Value	Lung model		
		Emphysematous	Normal	Restrictive
Peak airway pressure	minimum	descending	descending	descending
	maximum	ascending	ascending	ascending
Positive pleural pressure integral	minimum	ascending	ascending	ascending
	maximum	descending	descending	descending

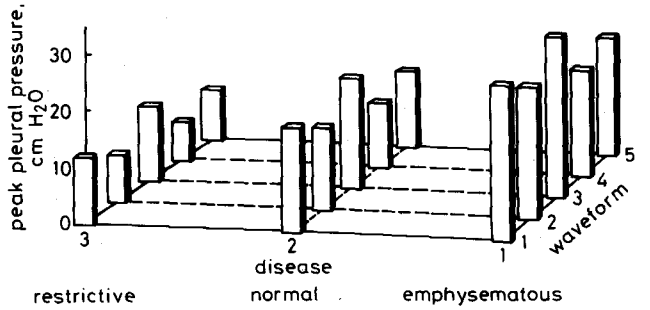

Fig. 8 *Volume ventilator: peak pleural pressure, cm H_2O. Waveforms: 1: sinusoid; 2: square; 3: ascending; 4: descending; 5: triangular*

The inspiratory pleural pressure cycle integral (PCI) was lower for the restrictive lung model than for the normal or the emphysematous models regardless of the waveform used (Fig. 9). For all lung models the minimum PCI was found using the ascending ramp and maximum PCI values were found using the descending ramp. The key results are summarised in Table 3.

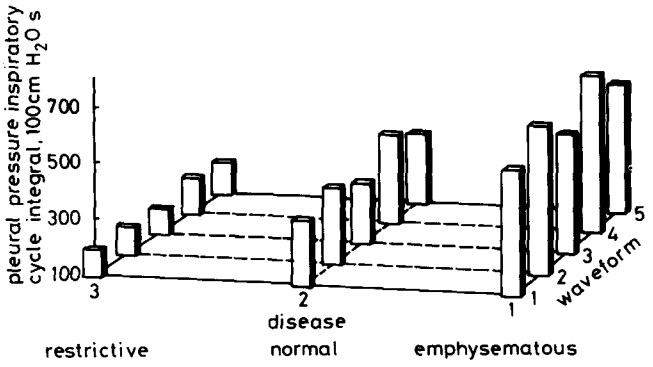

Fig. 9 *Volume ventilator: inspiratory pleural pressure positive cycle integral, 100 cm H_2O s. Waveforms: 1: sinusoid; 2: square; 3: ascending; 4: descending; 5: triangular*

5 Discussion

Our mathematical model of lung and chest wall dynamics simulates the intrathoracic pressures generated by mechanically assisted ventilation. This provides a quantitative basis for choosing ventilation patterns that minimise cardiopulmonary side effects. In our simulation studies we compared ventilatory patterns having the same tidal volume and rate. Theoretically, cardiovascular side effects could be avoided if pleural pressure did not become greater than its normal end-expiratory value. Because artificial ventilation applied at the airway opening cannot satisfy this requirement, we searched for an optimal waveform that minimises the inspiratory pleural pressure cycle integral (PCI). The likelihood of mechanically hazardous barotrauma can be minimised by preventing abnormally high values of the intrapulmonary pressures. Clinically applicable indices correlated with the likelihood of a barotrauma are the peak airway pressure (PAP) and flow (PAF). Thus, an optimal ventilator setting is one that supplies adequate ventilation at the lowest values of PCI, PAP and PAF. Using these indices, we compared simulations with five different waveforms of pressure- and volume-driven ventilators.

The ascending ramp, whether used with a pressure or a volume ventilator, produces the lowest PCI regardless of the lung model pathology. In contrast, for a volume ventilator, PAP is maximum for the ascending ramp. For the pressure ventilator, the minimum PAP was achieved with the square waveform. Therefore none of the waveforms examined here can simultaneously result in the lowest values of both PCI and PAP. Nevertheless, clinicians commonly try to minimise PAP while maintaining adequate ventilation. This strategy, however, may lead to a high PCI and cardiovascular side effects. With the availability of pleural pressure data, the clinical strategy should be altered.

To decide which waveform is most appropriate in clinical practice, we have to take into consideration the relative importance of the circulatory and respiratory side effects. For example, in a patient with an unstable haemodynamic state, the ascending wave will be preferable; however, in a patient having bulous emphysema, the square wave with a pressure ventilator or a descending ramp with a volume ventilator will be preferable.

In summary, choosing a ventilatory mode (i.e. the type of ventilator and the mechanical input function it delivers), requires consideration of the cardiopulmonary side effects. Using measurements of pleural and airway pressures, one can obtain quantitative indices that can serve as a guide for optimising the mechanical ventilation. Further theoretical and clinical studies are needed to build up an algorithm for attaining the optimal mode of ventilation of a specific patient.

Acknowledgment—This research was supported by grant 1293 from the Chief Scientist of the Israel Ministry of Health and in addition by the National Institutes of Health (HL-25830) in part. During the formative stages of this study, G. M. S. was a Henry Goldberg Visiting Professor of Biomedical Engineering at the Technion.

References

ADAMS, A. P., ECONOMIDES, A. P., FINLAY, W. I. and SYKES, M. K. (1970) The effect of variation of the inspiratory flow waveform on cardiorespiratory function during controlled ventilation in normo, hypo-, and hypervolaemic dogs. *Br. J. Anaesth.*, **42**, 818–825.

BARBINI, P. (1982) Non-linear model of the mechanics of breathing applied to the use and design of ventilators. *J. Biomed. Eng.*, **4**, 194–202.

BEN-HAIM, S. A. and SAIDEL, G. M. (1987) Chest wall mechanics: mathematical model and applications. *Fed. Proc.*, **46**, 819.

BERGMAN, N. A. (1963) Effect of different pressure breathing patterns on alveolar-arterial gradients in dogs. *J. Appl. Physiol.*, **18**, 1094–1052.

BERGMAN, N. A. (1967) Effect of varying respiratory waveforms on gas exchange. *Anesthesiol.*, **18**, 390–395.

BERGMAN, N. A. (1969) Effect of varying respiratory waveforms on distribution of inspired gas during artificial ventilation. *Am. Rev. Resp. Dis.*, **100**, 518–552.

BERGMAN, N. A. (1984) Fourier analysis of effects of varying pressure waveforms in electrical lung analogs. *Acta Anaesthesiol. Scand.*, **28,** 174–181.

BOROS, S. J. (1979) Variations in inspiratory:expiratory ratio and airway pressure waveform during mechanical ventilation: The significance of mean airway pressure. *J. Pediatr.*, **94,** 114–117.

CAMPELL, D. and BROWN, J. (1963) The electrical analogue of the lung. *Br. J. Anaesth.*, **35,** 684–693.

CASSIDY, S. S. and RAMANATHAN, M. (1984) Dimensional and analysis of the left ventricle during PEEP; relative septal and lateral wall displacements. *Am. J. Physiol.*, **15,** H792–H805.

DAMMAN, J. F., MCASLAN, T. C. and MAFFEO, C. J. (1978) Optimal flow patterns for mechanical ventilation of the lung. The effect of sine versus square wave flow pattern with and without an end-inspiratory pause on patients. *Crit. Care Med.*, **6,** 293–310.

FAIRLY, H. B. and BLENKARN, G. D. (1966) Effect on pulmonary gas exchange of variations in inspiratory flow rate during intermittent positive pressure ventilation. *Br. J. Anaesth.*, **38,** 320–328.

GOLDMAN, M. D. and MEAD, J. (1973) Mechanical interaction between the diaphragm and rib cage. *J. Appl. Physiol.*, **35,** 197–204.

HALL, S. V., JOHNSON, E. E. and HEDLEY-WHITE, J. (1974) Renal hemodynamics and function with continuous positive pressure ventilation in dogs. *Anesthesiol.*, **41,** 452–461.

HEMMER, M., VIQUERAT, C. E., SUTER, P. M. and VALLOTTON, M. B. (1980) Urinary anti-diuretic hormone excretion during mechanical ventilation and weaning in man. *Ibid.*, **52,** 395–400.

JANSSON, L. and JONSON, B. (1972) A theoretical study on flow patterns of ventilations. *Scand. J. Resp. Dis.*, **53,** 237–246.

JOHNSON, E. E., HEDLEY-WHYTE, J. and HALL, S. V. (1977) End-expiratory pressure ventilation and sulfobromophtalein, sodium excretion in dogs. *J. Appl. Physiol.*, **43,** 714–720.

LUCE, J. M. (1984) The cardiovascular effects of mechanical ventilation and positive end-expiratory pressure. *JAMA*, **252,** 807–811.

LUMLEY, J., MORGAN, M. and SYKES, M. K. (1969) Changes in arterial oxygenation and physiological dead space under anaesthesia. *Br. J. Anaesth.*, **41,** 279–287.

MEAD, J. and LORING, S. H. (1982) Analysis of volume displacement and length changes of the diaphragm during breathing. *J. Appl. Physiol.*, **53,** 750–755.

OWEN-THOMAS, J. B., ULAN, O. A. and SWYER, P. R. (1968) The effect of varying inspiratory gas flow rate on arterial oxygenation during IPPV in the respiratory distress syndrome. *Br. J. Anaesth.*, **40,** 493–502.

QVIST, J., PONTOPPIDANN, H., WILSON, R. S., LOWENSTEIN, E. and LAVER, M. B. (1975) Hemodynamic response to mechanical ventilation with PEEP. The effect of hyperemia. *Anesthesiol.*, **42,** 45–55.

RAHN, H., OTIS, A. B., CHADWICK, L. E. and FENN, W. O. (1946) The pressure-volume diagram of the thorax and lung. *Am. J. Physiol.*, **146,** 161–178.

RATTENBORG, C. C. and HOLADAY, D. A. (1966) Constant flow inflation of the lungs. Theoretical analysis. *Acta Anaesthesiol. Scand.*, **23,** Suppl., 211–223.

ROHER, F. (1915) Der Stromungswiderstand in den menschlichen Atemwegen und der Einfluss der unregelmassigen Verzweigung des Bronchialsystems auf den Atmungsverlauf verschiedenen Lungenbezirken. *Pflügers Arch. Gesamte Physiol. Menschen. Tiere.*, **162,** 225–229.

SYKES, M. K. and LUMLEY, J. (1969) The effect of varying inspiratory:expiratory ratios on gas exchange during anaesthesia for open heart surgery. *Br. J. Anaesth.*, **41,** 374–380.

VIQUERAT, C. E., RIGHETTI, A. and SUTTER, P. M. (1983) Biventricular volumes and function ventilated with PEEP. *Chest*, **83,** 509–514.